

Article

# Ultra-High-Capacity Optical Packet Switching Networks with Coherent Polarization Division Multiplexing QPSK/16QAM Modulation Formats

José Manuel Delgado Mendinueta \*, Satoshi Shinada, Hideaki Furukawa and Naoya Wada

Photonic Network System Laboratory, National Institute of Information and Communications Technology (NICT), 4-2-1 Nukui-Kitamachi, Koganei, Tokyo 184-8795, Japan; sshinada@nict.go.jp (S.S); furukawa@nict.go.jp (H.F); wada@nict.go.jp (N.W.)

\* Correspondence: mendi@nict.go.jp; Tel.: +81-42-327-6853

Received: 27 January 2017; Accepted: 31 March 2017; Published: 7 April 2017

**Abstract:** Optical packet switching (OPS) networks and its subsystems, like the burst-mode receiver, are an essential technology currently used in passive optical networks (PONs). Moreover, OPS may play a fundamental role on future hybrid optical circuit switching (OCS)/OPS networks and datacenter networks. This paper focuses on two fundamental subsystems of packetized optical networks: the digital coherent burst-mode receiver and the electro-optical switch. We describe and experimentally characterize a novel digital coherent burst-mode receiver that makes uses of the Stokes parametrization to rapidly estimate the state of polarization (SOP) and optimize the equalizer convergence time. This burst-mode receiver is suitable for optical packetized networks that make use of advanced modulation formats such as quadrature amplitude modulation (QAM). We study the suitability of (Pb,La)(Zr,La)O<sub>3</sub> (PLZT) optical switches for amplitude-variable coherent polarization division multiplexing (PDM) 16QAM modulation format and demonstrate a switching capacity of 10.24 Tb/s/port. We demonstrate a full 2 × 2 OPS node with a control plane capable of solving packet contention by means of packet dropping or buffering with a switching capacity of 10.24 Tb/s/port. Finally, we demonstrate the operation of the 2 × 2 OPS node with a record capacity of 12.8 Tb/s/port plus 100 km of dispersion-compensated fiber transmission.

**Keywords:** optical communications; optical packet-switched networks; coherent burst-mode receivers; PLZT optical switches

## 1. Introduction

Currently deployed optical networks are able to dynamically allocate network resources with a granularity of a wavelength channel in the so-called *fixed grid optical networks* [1], or, more recently, with some variability on the spectral width of each wavelength channel and adapting the modulation format in the *flexible/elastic optical networks* [2]. All these networks follow the connection oriented paradigm [3] and hence may collectively be referred to as optical circuit switching (OCS) networks [4]. Compared to static optical networks, where no optical switching is done, the flexibility in the wavelength dimension enables a better utilization of the network resources, a reduction of the energy consumption and lowering the costs [5]. In spite of this, it is expected that the increased demand of network capacity, which is likely to grow steadily over the following years [6], will push the requirements of optical networks even further. In order to meet these challenges, further increasing of the network granularity may be the key point to enhance the network utilization, reduce the energy consumption and lower the costs. In the past, the need to increase the network granularity motivated the emergence of optical packet switching (OPS) and optical burst switching (OBS) networks [7]. However, both OPS and OBS networks never abandoned the academic circles due to its great implementation

complexity and the ability of electronic switching to effectively compete with the benefits promised by OPS/OBS. Recently, research attention has been focused on hybrid optical networks [4]. These hybrid optical networks combine OCS *flexible/elastic lightpaths* for network services that require high availability with OPS *datagrams* [3] that deliver optical packets on a “best effort” approach. Hybrid OCS/OPS networks may make use of standard single mode fibers (SMFs) [4] or multicore fibers [8]. Moreover, OPS subsystems such as the burst-mode receiver with non-coherent on-off keying (OOK) modulation format are currently used in the upstream of optical access networks such as passive optical networks (PONs) [9] and upgraded coherent burst-mode receivers may play an important role in future datacenter networks [10,11]. Whether for hybrid OCS/OPS networks, PONs or datacenter networks, fast optical switching technologies and digital coherent burst-mode receivers are going to be essential technologies to leverage the development of optical networking over the next years.

Previously, extensive research has been carried out in our group on OPS-related subsystems. Our OPS node architecture has an all-optical data plane that is made of optical switches and fiber delay lines (FDLs). Owing to the optical switch transparency, optical packets with different data rates and high-order modulation formats can be handled without changing the OPS node architecture. Figure 1 shows an evolution of the OPS node capacity per port over time. Employing differential quaternary shift keying (DQPSK) modulated, fixed length, colored optical packets over 64 wavelength channels and a (Pb,La)(Zr,La)O<sub>3</sub> (PLZT) [12] optical switch with packet buffering, a switching capacity of 1.28 Tb/s/port was demonstrated [13]. Using polarization division multiplexing (PDM)-DQPSK modulation format, we demonstrated a switching capacity of 1.28 Tb/s/port with 32 wavelength channels [14] and later 2.56 Tbit/s/port with 64 wavelength channels [15,16].

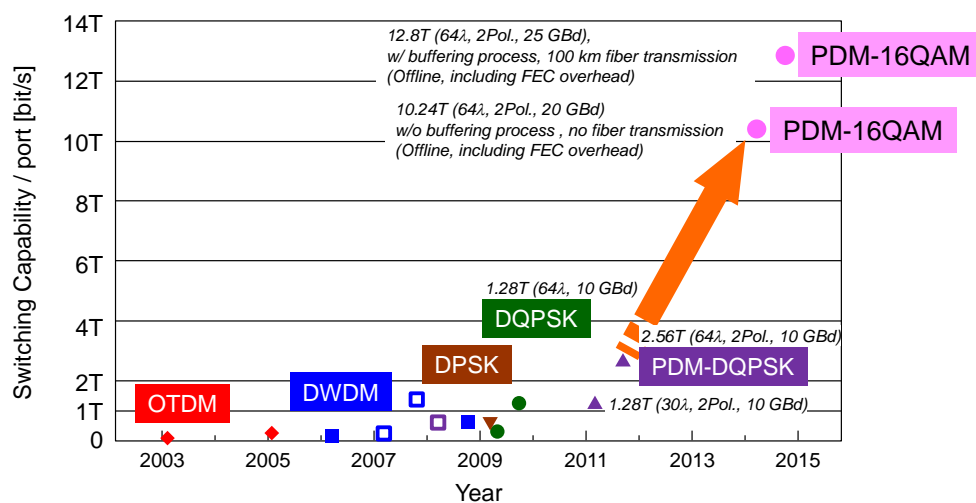


**Figure 1.** Evolution over time of the switching capacity of recent Optical packet switching (OPS) experiments at the National Institute of Information and Communications Technology (NICT).

In this paper, we will focus on the state-of-the-art optical switching subsystems that make use of wavelength division multiplexing (WDM) optical packets, advanced coherent modulation formats such as PDM-QPSK and PDM 16 quadrature amplitude modulation (QAM) and PLZT optical switches capable of switching multi-level QAM optical signals. On Section 2, we investigate the requirements of digital coherent burst-mode receivers (DCBMRXs) and describe a novel digital coherent burst-mode receiver that makes use of a state of polarization (SOP) estimator based on the Stokes parameters for rapid packet demodulation [17]. This receiver is an essential subsystem used in all the subsequent OPS demonstrations. Section 3 demonstrates a 10.24 Tb/s/port optical switch for PDM-16QAM optical packets [18]. One of the main aspects of optical switches for higher multi-level modulation format is transparency. A semiconductor optical amplifier (SOA) switch, which was often used as a time-division optical switch in the past, may cause serious distortion on multi-level QAM signals due

to the patterning effect [19,20]. To alleviate this, we employ electro-optical (EO) phase shift switches made of PLZT [12,18]. Additionally, the PLZT switch can provide a wider switching wavelength band than the SOA switches. Section 4 describes a full  $2 \times 2$  OPS optical switching node with a control plane capable of dealing with packet contention by means of packet dropping or packet buffering in fiber delay lines (FDLs). This  $2 \times 2$  OPS node is first demonstrated in back-to-back with a switching capacity of 10.24 Tb/s/port [21]. Section 5 demonstrates the  $2 \times 2$  OPS switching node with an improved transmitter and achieves 12.8 Tb/s/port in a transmission experiment consisting of two spans of 50 km of SMF and dispersion compensating fiber (DCF) [22]. Finally, the paper is summarized and the main conclusions are drawn.

## 2. Coherent Burst-Mode Receivers for PDM-QPSK and PDM-16QAM Modulated Payloads

The vast majority of current optical networks follow the connection oriented network paradigm and hence both transmitter and receiver work in continuous-mode from the beginning until the end of the connection [3]. For example, in a wavelength routed optical network (WRON), a wavelength channel named lightpath is open and remains open for the duration of the connection [1]. In dynamic optical networks, however, the information stream is packetized at the optical level, and this introduces a series of challenges in the optical receiver compared to the continuous-mode case.

A receiver capable of receiving optical packets is referred as a burst-mode receiver (BMRX) [23,24]. Current optical packet networks, such as PONs [9], make use of non-coherent, analog BMRXs with OOK modulation format [23]. The main challenges of OOK BMRXs are the detection of the presence of an incoming optical packet and the quick estimation of the amplitude of the optical signal to establish a threshold to cope with different packet amplitudes on a packet-by-packet basis. The introduction of coherent modulations requires digital coherent burst-mode receivers (DCBMRXs). Compared with analog BMRXs, DCBMRXs perform the signal processing in the digital domain and new parameters should be estimated, including the SOP, differential group delay (DGD), carrier frequency offset and carrier phase. Moreover, for PDM modulated signals, the quick estimation of the SOP is of extreme importance for correct signal demodulation and requires new algorithms to be developed for DCBMRXs. For example, in continuous-mode receivers, the constant modulus algorithm (CMA) has been proposed and widely accepted as a practical solution due to its low computational complexity [25]. However, depending on the initial equalizer kernel and the SOP of the optical packet, the CMA equalizer may converge to a situation when one of the polarizations is output to both tributaries. This situation is known as the CMA singularity [25]. This singularity problem is not critical on continuous-mode systems where it can be solved by inspecting the equalizer output and resetting the convergence process. Furthermore, the CMA equalizer may take several hundredths symbols to converge, which is not acceptable in a BMRX where the equalizer convergence should be as rapid as possible in order to increase the network throughput, i.e., reduce the optical layer packet overhead.

Several DCBMRX designs have been proposed in the literature to determine the SOP in a non-singular way. Ref. [26] transmits an optical packet header with only one polarization tributary and hence the SOP can be estimated with the algorithm proposed in [27]. However, this requires a more complex transmitter capable of nullifying one of the signal polarizations and additionally the lower energy in the packet header will impair the packet detection process due to additional noise compared to having a PDM header. Ref. [28] proposes to track the slope of the modulus of the CMA error signal, an operation that can be performed in parallel. However, this solution may have a high implementation complexity. In this section, we propose and experimentally characterize a novel DCBMRX that makes use of the Stokes parametrization in order to promptly initialize the equalizer with instantaneous convergence time and in a non-singular way.

### 2.1. Coherent Burst-Mode Receiver Based on the Stokes Sphere

Using the Jones notation, the received optical signal can be expressed as:

$$\begin{pmatrix} \tilde{X}' \\ \tilde{Y}' \end{pmatrix} = M \begin{pmatrix} \tilde{X} \\ \tilde{Y} \end{pmatrix} + N(t), \quad (1)$$

where  $\tilde{X}$  and  $\tilde{Y}$  are the complex envelopes of the two orthogonal transmitted polarizations,  $\tilde{X}'$  and  $\tilde{Y}'$  are the received complex envelopes and  $N(t) = [\tilde{n}_x(t) \ \tilde{n}_y(t)]^T$  is a complex additive white Gaussian noise (AWGN) added by active electrical and optical components to both polarizations. The matrix  $M$  models the polarization rotation and can be expressed as [29,30]:

$$M = \begin{pmatrix} \cos(\theta)e^{-i\varphi/2} & -\sin(\theta)e^{-i\varphi/2} \\ \sin(\theta)e^{+i\varphi/2} & \cos(\theta)e^{+i\varphi/2} \end{pmatrix}, \quad (2)$$

where the angles  $\theta$  in  $(-90^\circ, 90^\circ)$  and  $\varphi$  in  $(-180^\circ, 180^\circ)$  cover the whole Poincaré sphere. Note that this model does not include fiber attenuation losses, chromatic dispersion (CD), polarization dependent loss (PDL) and fiber nonlinearities [31]. The matrix  $M$  is unitary and hence its inverse is equal to its transpose conjugate. Consequently,  $M^{-1}$  can be trivially computed if an estimation of the values of the SOP rotation angles  $\theta$  and  $\varphi$  is known. The Stokes parameters of the received optical signal are defined as [32]:

$$\begin{aligned} s_0 &= |x|^2 + |y|^2, \\ s_1 &= |x|^2 - |y|^2, \\ s_2 &= 2 \cdot \text{Re}(x\bar{y}), \\ s_3 &= 2 \cdot \text{Im}(x\bar{y}). \end{aligned} \quad (3)$$

When plotted on the Poincaré sphere and for a PDM-QAM modulated signal, the Stokes transformation defines a lens-shaped object [33]. For an optical signal digitized at two samples per bit, each of the tributary components defines an eye diagram as illustrated on Figure 2a, where the clock recovery has placed the even samples at the center of the eye (the optimum sampling point) and the odd samples define the transition points. When plotted on the Stokes space, the even samples appear as a cluster of points located close to the sphere surface and the transition samples, i.e., the odd samples appear as smaller clusters with lower absolute value inside the sphere. For a PDM-QPSK modulated signal, the even samples produce four clusters of points on the sphere surface located on the vertexes of a square. High order QAM modulation formats produce clusters of points that approach the lens-shaped object [34]. This is illustrated on Figure 2d for a PDM-16QAM modulation. Note that the lens-shaped object defines a geodesic line on the Poincaré sphere and that this geodesic line defines an intersection plane with the sphere that can be characterized by a normal orthogonal vector  $\vec{n}$ .

The SOP rotation angles  $\theta$  and  $\varphi$  can be estimated by finding the best fitting plane for the set of points  $S = \{\vec{s}_i\}$ , where  $\vec{s} = (s_1, s_2, s_3)$  correspond to the points in the Stokes space given by the even samples of the signal. In this work, the singular value decomposition (SVD) [35] was used to estimate the vector  $\vec{n} = (n_1, n_2, n_3)$  normal to this plane. With the knowledge of  $\vec{n}$ , an estimation of the SOP rotation angles is given by:

$$\hat{\theta} = \frac{\tan^{-1} \sqrt{n_2^2 + n_3^2}}{n_1}, \quad (4)$$

$$\hat{\varphi} = \tan^{-1} \frac{n_3}{n_2}. \quad (5)$$

The SVD has a high computational cost. However, an accurate estimation of the angles  $\hat{\theta}$  and  $\hat{\varphi}$  can be obtained with only a reduced number of  $S$  points, which may reduce the overall complexity of the SOP estimator compared to alternative DCBMRX designs with iterative algorithms. With knowledge of  $\hat{\theta}$  and  $\hat{\varphi}$  and assuming a six-tap CMA equalizer (three symbols), the initial equalizer kernel is defined as:

$$\begin{aligned} H_{xx} &= \begin{bmatrix} 0 & 0 & 0 & \cos\theta e^{i\frac{\varphi}{2}} & 0 & 0 \end{bmatrix}, H_{xy} = \begin{bmatrix} 0 & 0 & 0 & \sin\theta e^{-i\frac{\varphi}{2}} & 0 & 0 \end{bmatrix}, \\ H_{yx} &= \begin{bmatrix} 0 & 0 & 0 & -\sin\theta e^{i\frac{\varphi}{2}} & 0 & 0 \end{bmatrix}, H_{yy} = \begin{bmatrix} 0 & 0 & 0 & \cos\theta e^{-i\frac{\varphi}{2}} & 0 & 0 \end{bmatrix}. \end{aligned} \quad (6)$$

Note that a CMA equalizer initialized with a kernel defined in the previous equation is singularity free and the convergence is instantaneous.

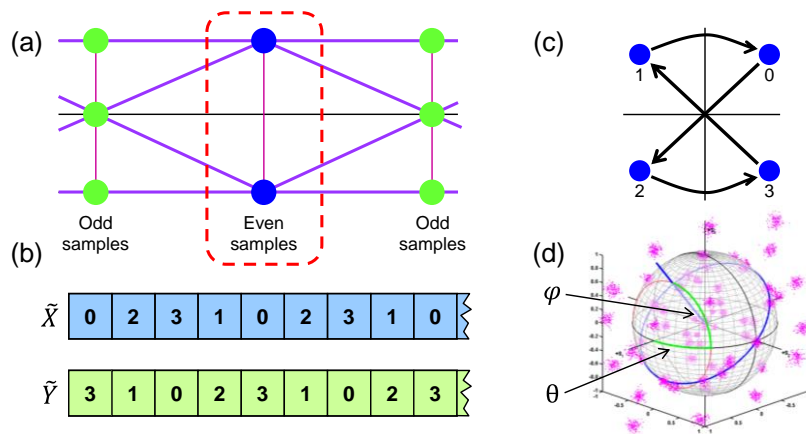


**Figure 2.** (a) Eye diagram for any of the tributary components of a PDM-QPSK signal, sampled at two samples-per-symbol; (b) format of the optical packet header. Each number represents the transmitted constellation symbol on each symbol period; (c) QPSK constellation diagram showing the constellation symbol mapping; and (d) example of the lens-shaped object for PDM-16QAM and a polarization rotation.

## 2.2. Digital Coherent Burst-Mode Receiver DSP Stages

Figure 3 shows a diagram of the digital signal processing (DSP) blocks used in the proposed DCBMRX [17]. First, a packet detector detects when an incoming optical packet arrives to the receiver and triggers the execution of the subsequent receiver stages [36]. Note that, in this work, this packet detector was not implemented and perfect packet detection was emulated with knowledge of the pattern timing from the transmitter. After the packet detector, a front-end correction and resampling stage corrects for channel skew and resamples the captured signal to four samples-per-symbol or the Nyquist rate of two samples-per-symbol. Then, the signal is normalized and the carrier frequency offset estimated and compensated by means of a fast Fourier transform (FFT). After the frequency offset has been removed, samples are aligned in a clock recovery stage using the Lee algorithm for two samples-per-symbol signals [37] or the Oerder algorithm for four samples-per-symbol signals [38]. Note that Nyquist shaped signals with small roll-off factor may require custom algorithms for clock recovery [39]. Next, the SOP angles  $\theta$  and  $\varphi$  are estimated using the proposed algorithm and its values used to initialize the CMA equalizer in case of receiving a PDM-QPSK modulation or a radially directed equalizer (RDE) for PDM-16QAM modulation. After equalization, the carrier phase is estimated with the Viterbi and Viterbi algorithm [40] or a set-partitioned Viterbi and Viterbi [41] for QPSK and 16QAM modulations, respectively. Finally, bit error rate (BER) is measured by error counting.

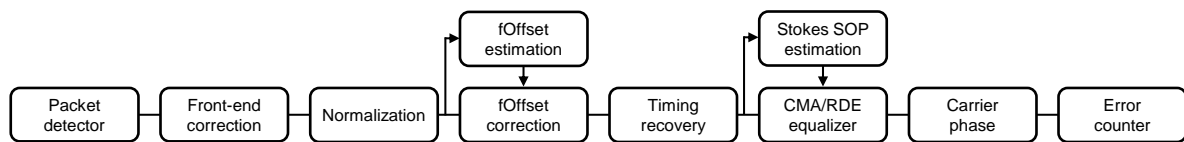


**Figure 3.** Digital signal processing (DSP) stages of the digital coherent burst-mode receiver.

### 2.3. Digital Coherent Burst-Mode Receiver Experimental Characterization

The experimental setup for the characterization of the coherent burst-mode receiver is shown in Figure 4a. The output of an external cavity laser (ECL) was split and modulated using two dual-parallel Mach-Zehnder modulators (DPMZM). These modulators were driven with four independent bit-streams at 10 Gb/s each to independently modulate every PDM-QPSK tributary component. Channels 2 and 4 included electrical phase delays and polarization X contained an optical delay line for precise aligning of the tributary components of the optical signal. After modulation, polarizations X and Y were combined in a polarization beam combiner (PBC). The PDM-QPSK optical signal was amplified using an erbium-doped fiber amplifier (EDFA), and, finally, and an optical attenuator was used to set the desired optical power before the optical receiver. The optical receiver consisted of an ECL free-running laser used as local oscillator (LO), a polarization-diverse optical hybrid plus balanced photodetectors, and a digital sampling oscilloscope used as a digitizer, having an electrical bandwidth of 16 GHz. The four electrical signals after the balanced photodiodes were digitized at 50 GS/s.

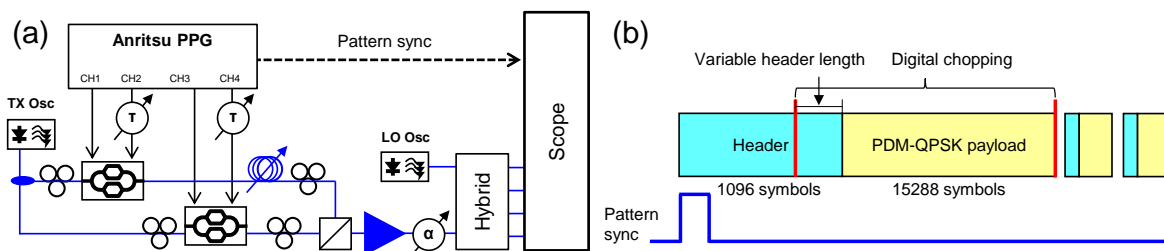


**Figure 4.** (a) Experimental setup for the characterization of the proposed coherent burst-mode receiver; and (b) diagram of the generated optical packets.

Figure 4b depicts a diagram of the generated optical packets used for the characterization of the burst-mode receiver. Each packet consisted of a header of 1096 symbols followed by a payload of 15,288 symbols. The pattern used on each payload binary tributary consisted of the first 15,288 bits of a pseudo-random binary sequence (PRBS) sequence of order 20 and the accumulated PRBS decorrelation between different tributaries was 262,144 bits. In the experimental setup of Figure 4a, no packet carver such as an acousto-optical modulator (AOM) or SOA was used. Instead, to simulate optical packets with a desired header length, the oscilloscope was triggered at the beginning of the pattern and then optical packets were digitally chopped with knowledge of the timing. The optical packet header consisted of two PDM tributaries, each repeating the constellation pattern shown in Figure 2b,c. This constellation has the property that the transitions to nullify optical power are maximized, which is beneficial for timing recovery. Furthermore, sufficient points in the Stokes space are generated for having an accurate estimation of the SOP.

### 2.4. Methodology and Experimental Results

Note that the experimental setup of Figure 4a does not include a polarization scrambler to rotate the SOP of the optical packets before the receiver. Instead, a set of 128 packets having a known SOP were captured, and then the SOP was estimated using the whole of the optical packet in order to

minimize the estimation errors, and the SOP was digitally corrected. Then, each packet was chopped to the desired header length and the SOP was digitally rotated using Equation (2) with  $\varphi$  in the range  $[-180^\circ, 180^\circ]$  and  $\theta$  in the range of  $[-90^\circ, 90^\circ]$  to simulate any arbitrary SOP rotation state over the whole Poincaré sphere. Before the digital SOP rotation, synthetic AWGN, independent for every optical packet and every SOP rotation, was added to the signal in order to produce a payload BER of roughly  $10^{-3}$ .

Figure 5a shows the averaged payload-BER of 128 optical packets as a function of the rotation angles  $\theta$  and  $\varphi$  covering the whole Poincaré sphere surface. In this case, no synthetic noise was added and the equalizer was a standard CMA equalizer initialized with taps:

$$\begin{aligned} H_{xx} = H_{yy} &= [0\ 0\ 0\ 1\ 0\ 0], \\ H_{xy} = H_{yx} &= [0\ 0\ 0\ 0\ 0\ 0]. \end{aligned} \tag{7}$$

Inspection of Figure 5a clearly reveals that the CMA equalizer exhibits a singularity when the SOP rotation angle is  $\theta = [+45^\circ, -45^\circ]$  for any value of  $\varphi$ . We repeated this measurement and added synthetic noise to the experimental data with a power such as the payload-BER equaled the forward error correction (FEC) limit of  $10^{-3}$ . Figure 5b shows that the effect of noise, compared to Figure 5a, is to unsmooth the curves, but the CMA equalizer singularity is still present. Next, the proposed SOP estimation and equalizer initialization algorithm were tested for header sizes of {4, 8, 16, 32, 64} samples. The results of this measurement are plotted in Figure 5c. Inspection of the figure reveals that the average BER stays in a range of approximately  $[10^{-3}, 5 \times 10^{-3}]$ , independently of the header size, which demonstrates that the proposed algorithm solves the CMA singularity problem.

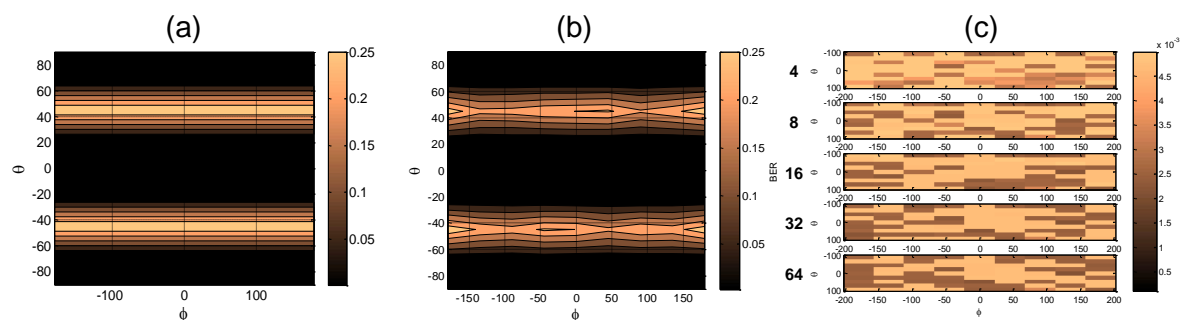


**Figure 5.** (a) BER probability as a function of the SOP angles  $\theta$  and  $\varphi$  for the standard CMA algorithm and no additional noise, (b) same as (a) but with synthetic AWGN, and (c) same parameters as (a) but for the proposed algorithm and varying-size header lengths.

Finally, we assessed the equalizer convergence time by doing a time-resolved BER measurement averaging the errors of each of the four PDM-QPSK PRBS tributaries over the 128 captured packets. Figure 6a shows the time-resolved BER in the packet payload, for the standard CMA receiver and the proposed new receiver algorithm, averaged over all SOP rotations covering the Poincaré sphere. The red line shows the average BER for all 128 packets without any SOP rotation and can be considered as the calibrated BER value. For the standard CMA receiver, all the cases where the singularity was detected were not computed in order to not artificially increase the number of errors. Figure 6b shows the curves of Figure 6a filtered with a median filter having a window size of 31 to smooth the curves. Results demonstrate that, on average, the CMA receiver takes up to 3000 symbols to converge. However, the CMA equalizer initialized with the algorithm proposed in this work converges instantly for an estimation size of 16 or greater and completely avoids the singularity problem. Under a noise loading that yields a payload BER of  $10^{-3}$ , initialization of the CMA equalizer is successful with only 16 estimation points of the packet header.

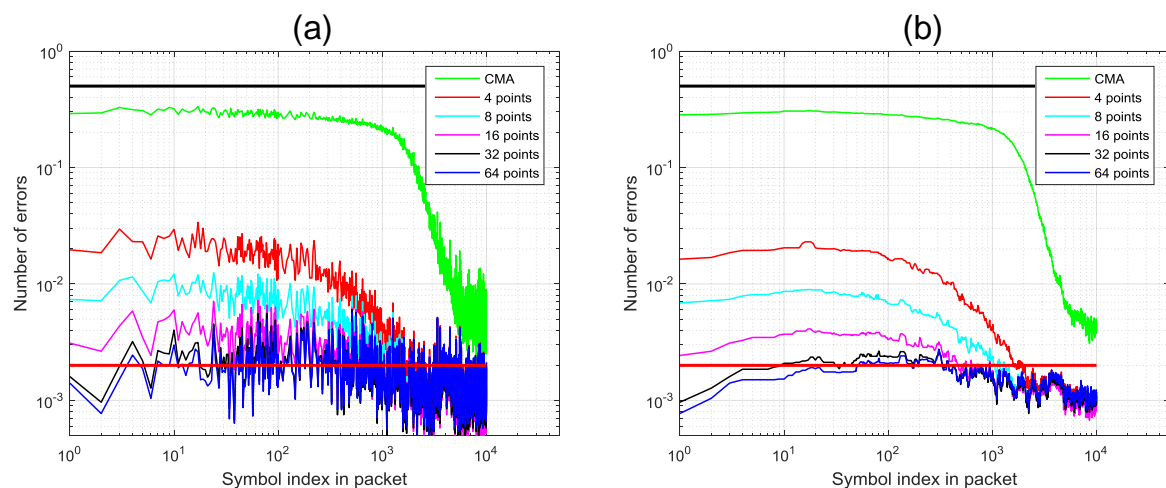


**Figure 6.** (a) time-resolved BER measurement of the packet payload; (b) same as (a), but a median filter has been applied to smooth the curves.

### 3. High-Capacity DWDM PDM-16QAM Optical Switch

This section describes the first experimental demonstration of a high-capacity dense wavelength division multiplexing (DWDM) optical packet switching node using PDM-16QAM modulated optical packets and electro-optical PLZT switches.

#### 3.1. Experimental Setup

Figure 7 shows the experimental setup of a transmitter for DWDM, PDM-16QAM-modulated optical packets. As light sources, we used an array of 64 lasers, ranging from 1537.0 to 1562.23 nm on the 50 GHz grid spacing. The continuous waves of the 32 odd and 32 even channels were collectively modulated by two independent DPMZMs, respectively. The modulators generated 20 Gbd single polarization 16-QAM optical packets with an aggregated bit rate of 80 Gbit/s per channel and per polarization. To generate the optical packet train, the continuously modulated signal was gated by two MZM modulators to remove the bogus PRBS data used in the guard time between packets. Then, packets were polarization-multiplexed by a polarization beam combiner (PBC) with a decorrelation of 12 symbols between polarizations. As a result, waveband optical packets at a rate of 10.24 Tbit/s were generated.

A train of eight packets of different lengths, ranging from 1000 to 4000 symbols, was generated and each packet had either a PSK label A or label B, as shown in the inset of Figure 7. For label generation, 10 GHz optical pulses generated by a mode-locked laser diode (MLLD, 1530 nm) were modulated using known timing from the coherent packets payload pattern by an intensity modulator. The pulses were input to a 200 Gchip/s multiple optical encoder (MOE) to generate optical phase-shift keying (PSK) codes. The MOE has an AWG configuration [42,43] with 16 inputs and 16 outputs, and behaves like a transversal filter to simultaneously generate 16-chip PSK codes. When a short pulse is sent into one of input ports of MOE, 16 different PSK codes are generated from each output port [43]. In this demonstration, two PSK codes were chosen and named label A and label B. After coupling of even and odd channels by a wavelength interleaver (100 GHz to 50 GHz), each packet was sandwiched by the PSK labels.

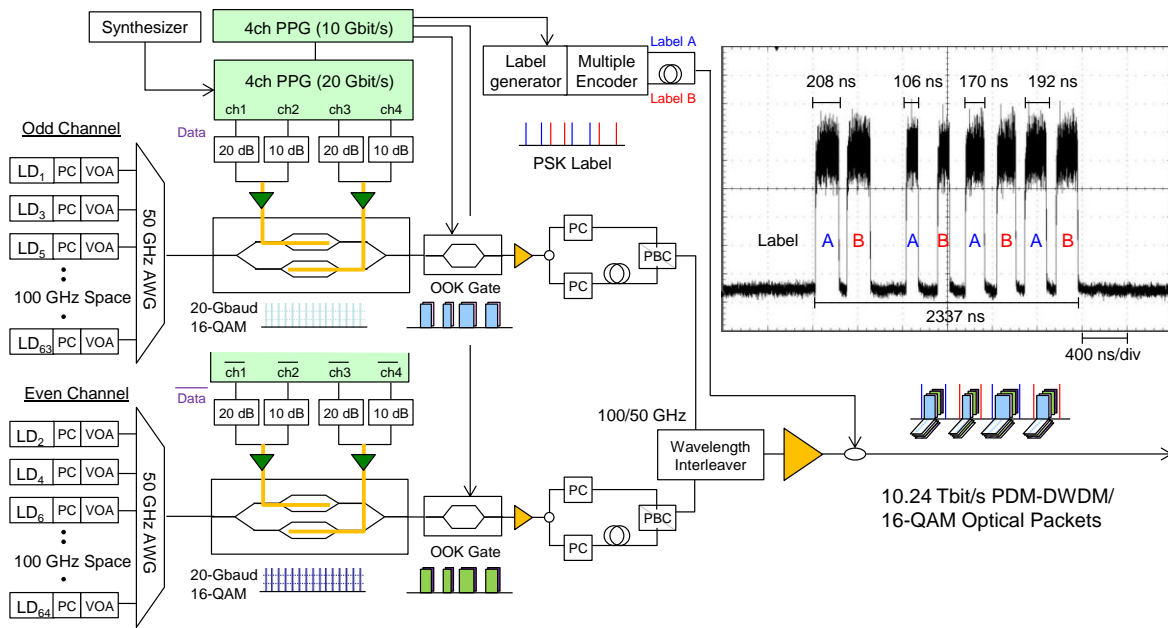


**Figure 7.** Transmitter setup for the generation of DWDM PDM-16QAM modulated optical packets and 64 wavelength channels, (inset) diagram of the generated eight-packet train.

The packet train was then split into two to simulate two different transmitters, named TX1 and TX2, as shown in Figure 8. In this experiment, we used two  $1 \times 2$  PLZT switches for the label-switching ( $2 \times 2$  OPS without buffer), designed to forward optical packets with label A only input from TX1 and TX2. Each  $1 \times 2$  PLZT optical switch had a PDL ranging from 0.3 to 1 dB. When multiple optical decoders (MODs) [42,43] recognized an input label as label A, an output gate signals an FPGA based buffer manager. The buffer manager sends open or close signals to two switches for TX1 and TX2. As a result, four-packet trains with label A were output to each port. To demonstrate a packet addition process, a delayed four-packet train of TX2 was added to a four-packet train of TX1. Output packets after the packet addition process were input to a polarization-diverse coherent receiver, shown in Figure 8, using a free-running tunable laser as local oscillator (LO) with linewidth of approximately 100 kHz. The four-channel electrical signal after photo detection was then digitized at 50 GS/s, and the offline processing was performed with MATLAB (version R2015b, The MathWorks, Inc., Natick, MA, USA) for easy prototyping.

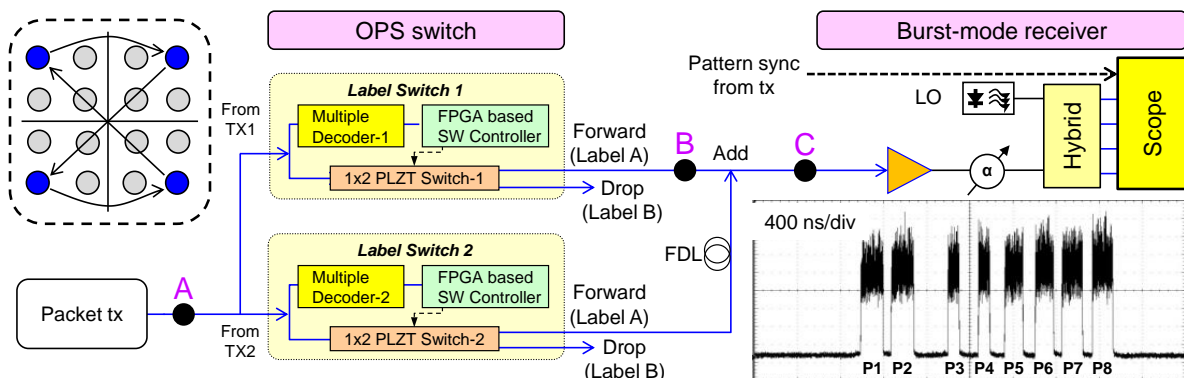
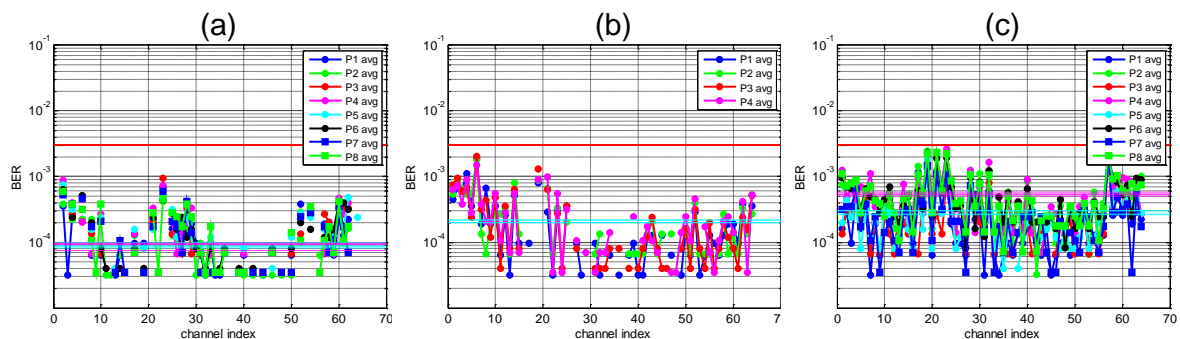


**Figure 8.** Experimental setup of the optical packet switching node, configured to forward packets with label A and drop packets with label B. (insets) Constellation diagram of the packet header and waveform of the received eight packets.

The inset of Figure 8 shows a diagram of the optical packet train at the receiver. Each optical packet had a header of 64 symbols (128 samples) followed by a variable-length PDM-16QAM payload. The optical packet header consisted of two PDM tributaries, each modulating the outermost ring of the 16-QAM constellation as shown in the inset of Figure 8. Optical packet detection was not considered in this experiment and known timing from the transmitter was used to digitally chop the optical packets for further DSP processing, thus simulating a null packet error rate (PER). The main difference of this receiver with the one described in Section 2.2 is an extra retiming stage necessary for quickly compensating for DGD. It was found that packets P2, P4, P6 and P8, after switching, had a significant amount of DGD compared with packets P1, P3, P5 and P7. In order to digitally compensate this, SOP was reverted with a one-tap butterfly structure, and then the Lee algorithm [37] was employed to realign both polarizations before the RDE equalizer.

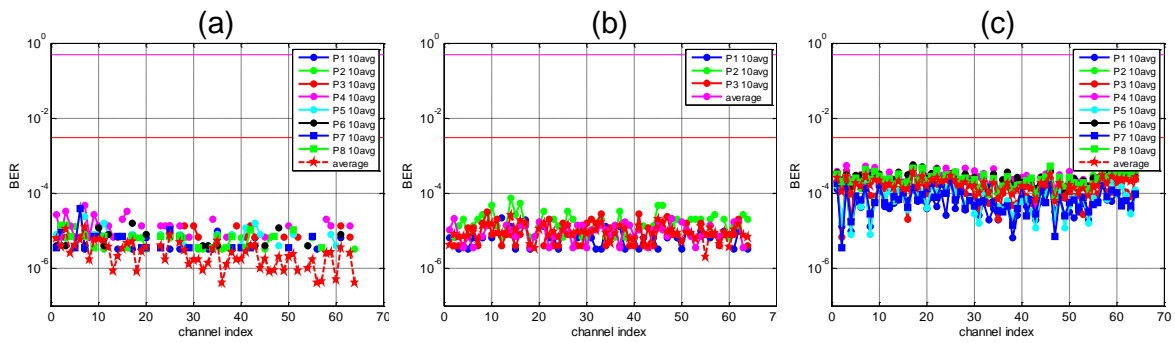
### 3.2. Experimental Results and Discussion

Figure 9a–c shows the bit-error-rate (BER) for the 64 wavelength channels after the transmitter (back-to-back, measured at point A on Figure 8), after label-switching (measured at point B) and after packet addition (measured at point C), respectively, for every individual packet P1 to P8 and each measurement averaged over three packets (best three of 10 experimental trials). Discontinuities in the plots arise from error-free measurements. The observed saw-tooth shape is due to uneven biasing of the inphase-quadrature (IQ) modulator between odd and even channels and also to modulator BIAS instabilities. These plots show that PDM-16QAM payload BER is below the FEC limit of  $3 \times 10^{-3}$ . Moreover, the soft horizontal lines show the total BER averaged for all odd packets (cyan) and even packets (magenta), showing a very small BER penalty after label-switching. However, after the addition of packets, even packets in the packet train suffer an additional penalty due to increased DGD originating in the optical switch.



**Figure 9.** (a) Back-to-back payload BER for optical packets P1–P8 as a function of the wavelength channel measured at point A in the setup of Figure 8; (b) payload BER after optical switching and label swapping measured at point B of Figure 8; (c) payload BER after packet addition measured at point C on Figure 8.

Next, we optimized the OPS transmitter by placing the packet carving MZMs in front of the modulator (instead of after the modulators) and optimized the DPMZMs BIAS. The average was computed over 10 traces. Figure 10 shows a significant BER improvement compared to Figure 9 and demonstrates the successful switching with a capacity of 10.24 Tbit/s/port. We confirmed that the OPS node processing using PLZT optical switches did not adversely affect the multi-level PDM-16QAM modulated optical packet signals.



**Figure 10.** Improved BER measurements with respect to Figure 9. (a) Back-to-back payload BER for optical packets P1-P8 as a function of the wavelength channel measured at point A in the setup of Figure 8; (b) payload BER after optical switching and label swapping measured at point B in Figure 8; (c) payload BER after packet addition measured at point C in Figure 8.

#### 4. High Capacity 2 × 2 OPS Node with Contention Resolution

In this section, we characterize a 2 × 2 OPS node, shown in Figure 11a, with two strategies to deal with packet contention: optical buffering with FDLs and packet dropping. In the control plane, the label processor consists of multiple optical decoders [42,43] that recognize an input label and send triggering signals to a buffer manager implemented on a field programmable gate array (FPGA) [44,45]. The label generation process is described on Section 3.1. The buffer manager is able to electronically control the optical switch matrix to perform packet forwarding, packet dropping or packet buffering. The optically transparent data plane uses one 1 × 8 PZLT optical switch on each input port. This 2 × 2 OPS node will be the key subsystem in the packet contention resolution experiment of this section and in the packet transmission plus a switching experiment of Section 5.

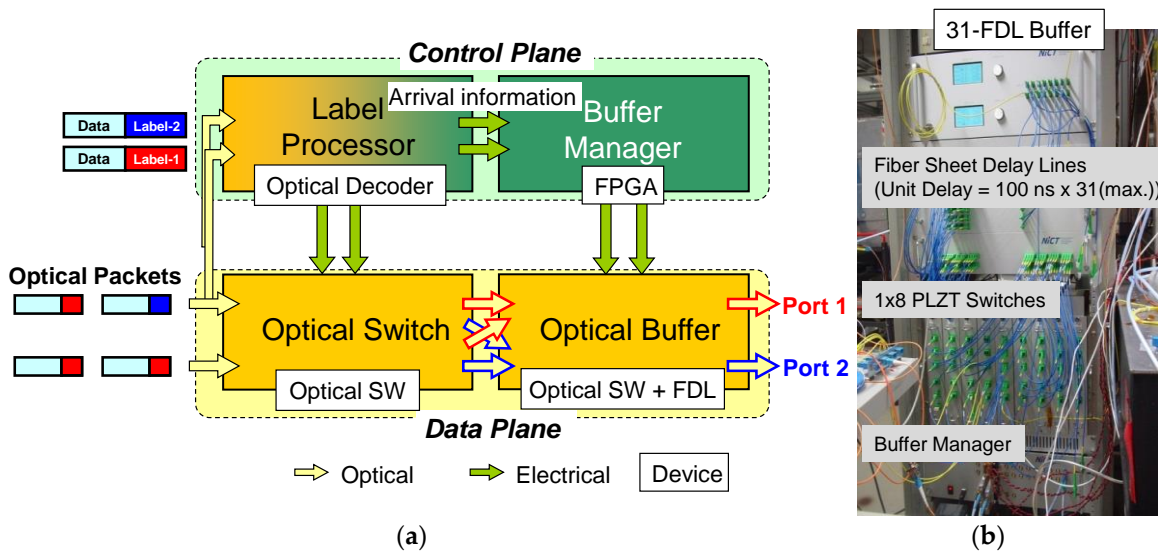


**Figure 11.** (a) architecture of the 2 × 2 optical switching node with contention resolution by packet dropping and optical packet buffering; (b) picture of the 2 × 2 OPS node prototype.

##### 4.1. Switching and Buffering Experimental Setup

In this experiment, we used the same optical packet transmitter described in Section 3.1. After the transmitter, the eight-packet train was split in a 1 × 2 splitter to simulate two different transmitters named TX1 and TX2, and both TX1 and TX2 were input to the optical switching node, as shown in Figure 12. We reconfigured our 31-FDL buffering system, which consisted of nine 1 × 8 PLZT switches,

fiber sheet delay lines (FSDLs) and an FPGA-based buffer manager, and made a  $2 \times 2$  OPS node system where two PLZT switches were followed by three FSDLs. The unit delay time of each FSDL was 100 ns. One of three different delays {0, 100, 200} ns was given to the packet by changing an output port of the switch. In this demonstration, only packets with label A were processed and characterized. When the multiple optical decoders [42,43] recognized an input label as label A, gate signals output the optical packet to the buffer manager. The buffer manager can resolve a maximum contention of  $4 \times 1$  packets.

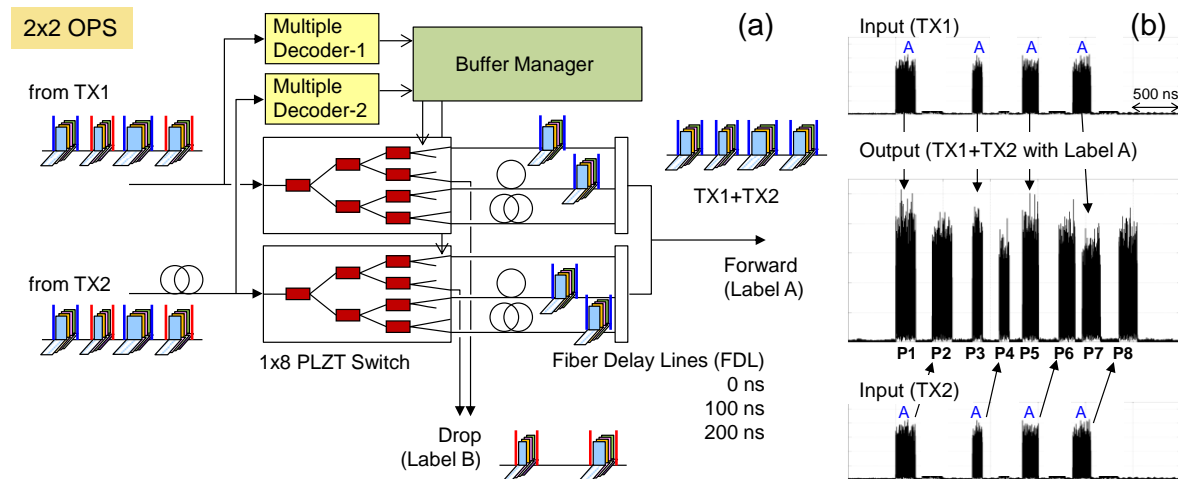


**Figure 12.** (a) experimental setup of the  $2 \times 2$  optical packet switch one drop line and three fiber sheet delay lines; (b) schematic of the optical packet trains at the output of each optical switch and the aggregated packet train to be processed by the receiver.

The aggregated output packets after the OPS node were input into a polarization-diverse coherent receiver, shown in Figure 8, using a free-running tunable laser as local oscillator (LO) with linewidth of approximately 100 kHz (the combined linewidth of TX plus RX was approximately  $\sim 200$  kHz). The four-channel electrical signal was then digitized at 50 GS/s and the offline processing was performed with MATLAB with a DCBMRX as described in Sections 2.2 and 3.1. Figure 12b shows a diagram of the optical packets used in the experiment, consisting of an optical header of 64 symbols followed by a variable-length PDM-16QAM payload. The format of the received optical packet train and the methodology for processing them was similar to the one described on Section 3.1.

#### 4.2. Experimental Results and Discussion

In the optical switch, optical packets with label B were dropped and packet contentions between packets with label A of TX1 and TX2 were resolved. In this designed packet contentions, four packets with label A of TX1 and TX2 were given a delay of {0, 0, 0, 100} ns and {100, 0, 100, 200} ns, respectively. All packets with label A were output successfully without overlapping. Figure 13 shows the measured BER for the entire 64 wavelength channels after the OPS node, for every individual packet (P1 to P8) and averaged over 10 packets from different experimental realizations. The observed saw-tooth shape is due to uneven biasing of the DPMZMs between odd and even channels. These plot show that the payload BER is below the FEC limit of  $3 \times 10^{-3}$  after the OPS node and demonstrates the successful operation of the  $2 \times 2$  OPS node including packet buffering with a capacity of 12.24 Tb/s/port.

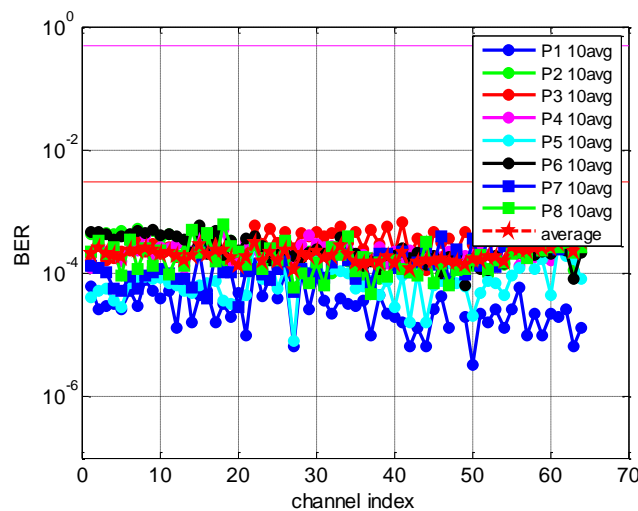


**Figure 13.** BER of the 64 wavelength channels after buffering in the OPS node for each of the eight packets with label A from TX1 and TX2, shown Figure 12b.

## 5. High Capacity $2 \times 2$ OPS Node with Contention Resolution and Fiber Transmission

This section describes the most up-to-date OPS experiment with a record capacity of 12.8 Tb/s/port. Compared to Section 4, we used an improved transmitter setup and the optical packet signal was transmitted over 100 km of dispersion compensated SMF.

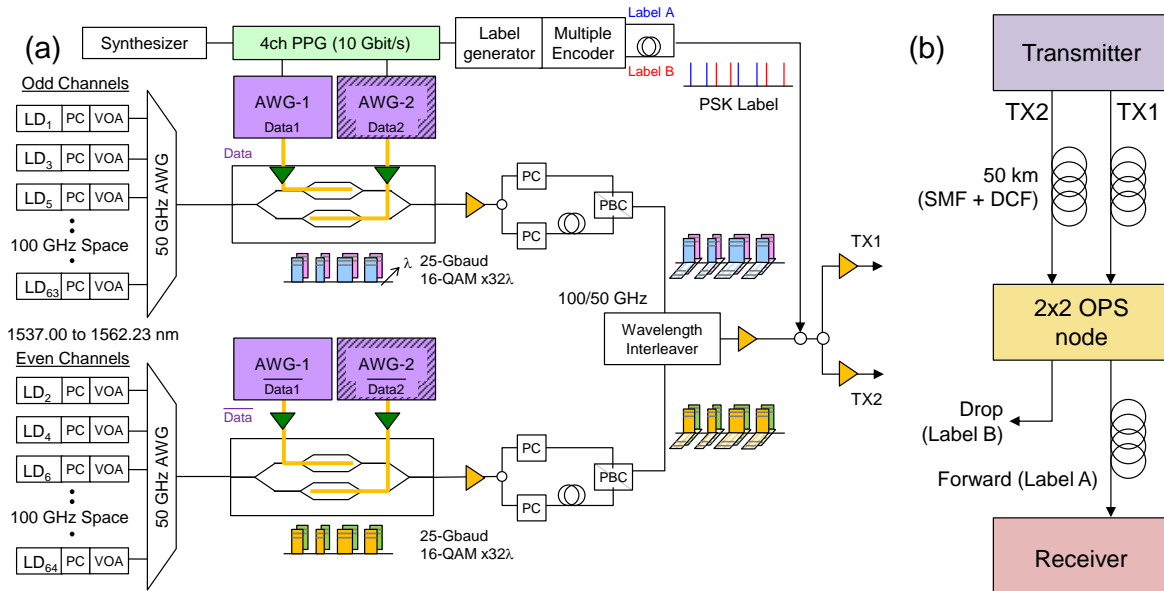
### 5.1. Transmission Experimental Setup

Figure 14 shows the experimental setup of a transmitter for DWDM PDM-16-QAM optical packets. Compared with the setup introduced in Figure 7, the improved setup of Figure 14 introduces two enhancements. First, arbitrary waveform generators (AWGs) were used to generate the driving signal for the modulators as opposed to two-bit digital to analog converters (DACs) made of discrete components. Secondly, the AWGs were used to carve the signal in order to generate the optical packets and the OOK gate based on an MZM was removed from the setup.

The AWGs used to drive the modulators had an electrical bandwidth of 16 GHz and a resolution of eight bits. The four-level I and Q electrical tributaries input to the modulator were equalized with a Nyquist 128-symbol square root raised cosine (SRRC) filter with a roll-off factor of 0.25, followed by a 1025-tap pre-emphasis filter to compensate for the DACs' non-ideal frequency response. Notably, additional MZM modulators were not used in this work to carve the continuous wave (CW) signal into optical packets owing to the ability of the AWGs to set both I and Q tributaries to the null point of the DPMZMs. The data rate of the optical packets was increased from 160 Gb/s to 200 Gb/s and the decorrelation between the X and Y polarization was six symbols, in order to yield a total capacity of 12.8 Tbit/s. The back-to-back error vector magnitude of the generated PDM-16QAM signal was about 10% without any receiver equalization (with the exception of the receiver's matched SRRC filter). The format of the optical packet train and packet labels after the transmitter was similar to the one shown on the inset of Figure 7. After the transmitter, the optical signal was split into two to simulate two transmitters, named TX1 and TX2.

After the transmitter, the set of eight packets from TX1 and TX2 were propagated through different 50 km SMFs plus DCF spans and were input to both input ports of the  $2 \times 2$  OPS node, described in Section 4. In this experiment, the OPS node was configured to forward optical packets with label A of TX1 and TX2 to the same output port in order to emulate packet contention. To resolve this packet contention, FDLs were used as an optical buffer. The buffer manager calculated the delay time required for each packet to avoid collisions and controlled a set of PLZT switching matrices to send each packet to appropriate FDLs having 0, 100 and 200 ns, respectively. On the other hand, optical packets with

label B (only from TX2) were sent to the alternative output port without the buffering process (drop process). This whole processing is illustrated in Figure 15, which shows the waveforms processed in the data plane of the OPS node. In the label switching process, packets with label A and label B were separated and four packets with label B of TX2 were output (marked in Figure 15 as DROP). Optical packets with label A were output after the buffering process without any packet loss (labelled FORWARD on Figure 15).



**Figure 14.** General experimental description/setup of the packet buffering and transmission experiment. (a) Packet transmitter; and (b) general diagram of the OPS transmission experimental setup.

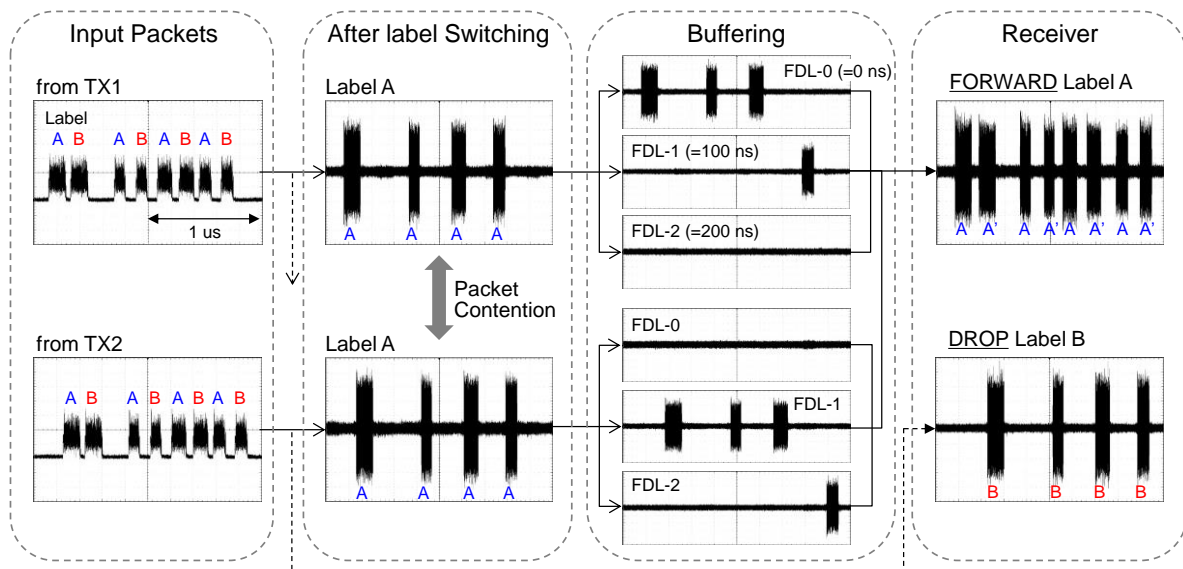


**Figure 15.** Waveforms of the packets processed in the 2 × 2 OPS node. DROP and FORWARD, along with back-to-back, were the waveforms at the input of the coherent receiver (ECOC 2014).

The optical packets were received by a polarization diverse coherent receiver followed by a digitizer as described in Section 3.1. Asynchronous optical packet detection was not considered in this experiment and known timing from the transmitter was used to digitally chop the optical

packets for further DSP processing, simulating a null PER. The DSP blocks were similar to the ones described in Section 2.2, with the difference that, after normalization, the digital signal was filtered with a matched SRRC filter similar to the one used in the transmitter. Then, the signal was upsampled to four samples-per-symbol for timing recovery using the delay multiplication algorithm [46], which is appropriated for Nyquist pulse-shaped signals. After timing recovery performed at four samples-per-symbol, the signal was downsampled to two samples-per-symbol for subsequent processing.

### 5.2. Packet Switching, Buffering and Transmission Results and Discussion

BER measurements of back-to-back, after the packet dropping process (named DROP in Figure 15) and after the packet forwarding process (named FORWARD) are shown in Figure 16a–c, respectively. The BER for every individual packet was averaged over 10 captured packets. Discontinuities in the plots of back-to-back arise from error-free measurements. Deterioration of BER after the packet dropping was caused by a large insertion loss of the PLZT switch and couplers (about 18 dB). The BER after the forwarding process was kept below the FEC limit of  $3 \times 10^{-3}$ . However, due to crosstalk between output ports of the optical switch, residual packets were output in the undesired delay lines. As a result of the interference between signals and residual signals after the couplers, a severe deterioration occurred. In contrast, the drop process without the buffering had no such interferences, and, consequently, BER was much lower than in the forward process. The improvement of the OPS node crosstalk characteristics is still an issue to be tackled in future work. These results successfully demonstrate the operation of a 12.8 Tbit/s optical packet switching node with buffering after 50 km of fiber transmission. Even after the signal propagation, DWDM PDM-16QAM optical packets could be correctly handled by the  $2 \times 2$  OPS node consisting of low polarization dependent, wideband PLZT optical switches.

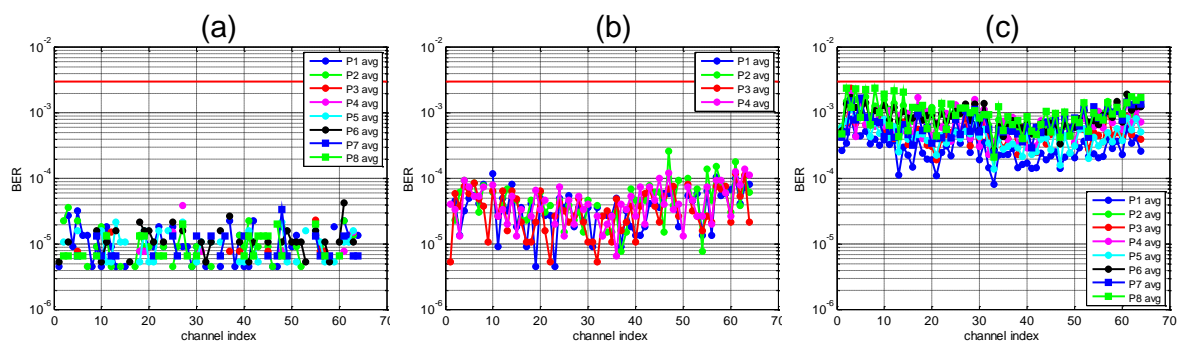


**Figure 16.** BER of 64 wavelength channels (a) back to back (b) after dropping packets (marked as DROP in Figure 15) and (c) after the packet forwarding process (marked as FORWARD in Figure 15).

## 6. Conclusions

We have reviewed the current state-of-the-art of OPS technologies using coherently modulated PDM-QPSK/PDM-16QAM optical packets with special attention on the digital coherent burst-mode receiver and the electro-optical PLZT optical switch subsystems and have characterized a complete  $2 \times 2$  OPS node with a control plane capable of resolve packet contention by dropping or buffering. We have proposed and experimentally demonstrated a novel DCBMRX that makes use of the Stokes parameters to promptly estimate the SOP. The estimator makes use of the SVD decomposition and an estimator of size 16 is enough to guarantee a packet payload at the FEC limit of  $10^{-3}$  and this may reduce the overall complexity of the receiver. We have also experimentally demonstrated the suitability of PLZT optical switches as a subsystem for the switching of high-order QAM modulated optical packets. Using a transmitter with a two-bit DAC made of discrete components to generate PDM-16QAM modulated optical packets, we demonstrated a switching capacity of over

10.24 Tb/s/port. We used the PLZT optical switch as a building block for a full  $2 \times 2$  OPS node with packet contention resolution by packet dropping or packet buffering in FDLs. We first evaluated this optical switch in a back-to-back to demonstrate the node operation with packet buffering at 10.24 Tb/s/port. Finally, we increased the switching capacity to 12.8 Tb/s/port and transmitted the OPS signal through two spans of 50 km of dispersion compensated SMF, owing to an improved packet transmitter consisting of eight-bit AWGs, which did not require a packet carver.

**Acknowledgments:** The authors would like to thank Takeshi Makino and Takahiro Hashimoto for their technical support during the experimental work.

**Author Contributions:** J.M.D.M. and S.S. conceived and designed the experiments; J.M.D.M. performed the experiment described in Section 2; J.M.D.M. and S.S. performed the experiments described in Sections 3–5; all authors were involved in the discussion of the results; J.M.D.M. and S.S. wrote the manuscript and prepared the figures; and all authors reviewed the manuscript and approved it for publication.

**Conflicts of Interest:** The authors declare no conflict of interest.

## References

1. Ruiz, M.; Lord, A.; Fonseca, D.; Pioro, M.; Wessaly, R.; Fernandez-Palacios, J.P. Planning Fixed to Flexgrid Gradual Migration: Drivers and Open Issues. *IEEE Commun. Mag.* **2014**, *52*, 70–76. [[CrossRef](#)]
2. Tomkos, I.; Azodolmolky, S.; Sole-Pareta, J.; Careglio, D.; Palkopoulou, E. A Tutorial on the Flexible Optical Networking Paradigm: State of the Art, Trends, and Research Challenges. *Proc. IEEE* **2014**, *102*, 1317–1337. [[CrossRef](#)]
3. Tanenbaum, A.S. *Computer Networks*, 4rd ed.; Prentice Hall: Upper Saddle River, NJ, USA, 2002.
4. Furukawa, H.; Miyazawa, T.; Wada, N.; Harai, H. Moving the boundary between wavelength resources in optical packet and circuit integrated ring network. *Opt. Express* **2014**, *22*, 47–54. [[CrossRef](#)] [[PubMed](#)]
5. Zapata-Beghelli, A.; Bayvel, P. Dynamic versus Static Wavelength-Routed Optical Networks. *J. Lightwave Technol.* **2008**, *26*, 3403–3415. [[CrossRef](#)]
6. Cisco Systems, Inc. The Zettabyte Era: Trends and Analysis. In *White Paper*; Cisco Systems, Inc.: San Jose, CA, USA, 2016.
7. Jue, J.P.; Yang, W.-H.; Kim, Y.-C.; Zhang, Q. Optical packet and burst switched networks: A review. *IET Commun.* **2009**, *3*, 334–352. [[CrossRef](#)]
8. Amaya, N.; Irfan, M.; Zervas, G.; Nejabati, R.; Simeonidou, D.; Sakaguchi, J.; Klaus, W.; Puttnam, B.J.; Miyazawa, T.; Awaji, Y.; et al. Fully-elastic multi-granular network with space/frequency/time switching using multi-core fibres and programmable optical nodes. *Opt. Express* **2013**, *21*, 8865–8872. [[CrossRef](#)] [[PubMed](#)]
9. Effenberger, F.; El-Bawab, T.S. Passive Optical Networks: Past, present, and future. *Opt. Switch. Netw.* **2009**, *6*, 143–150. [[CrossRef](#)]
10. Miao, W.; Yin, X.; Bauwelinck, J.; Dorren, H.; Calabretta, N. Performance Assessment of Optical Packet Switching System with Burst-mode Receivers for Intra-data Center Networks. In Proceedings of the Optical Fiber Communications Conference (OFC), San Francisco, CA, USA, 9–13 March 2014.
11. Mestre, M.A.; de Valicourt, G.; Jenneve, P.; Mardoyan, H.; Bigo, S.; Pointurier, Y. Optical Slot Switching-Based Datacenters with Elastic Burst-Mode Coherent Transponders. In Proceedings of the European Conference on Optical Communications (ECOC), Cannes, France, 21–25 September 2014.
12. Nashimoto, K.; Kudzuma, D.; Han, H. Nano-Second Response, Polarization Insensitive and Low-Power Consumption PLZT  $4 \times 4$  Matrix Optical Switch. In Proceedings of the Optical Fiber Communications Conference (OFC), Los Angeles, CA, USA, 6–10 March 2011.
13. Shinada, S.; Furukawa, H.; Nakamura, M.; Wada, N. Record Switching Throughput of 1.28 Tb/s/port (64-wavelength  $\times$  20-Gbit/s) by DWDM/NRZ-DQPSK Optical Packet Switching. In Proceedings of the European Conference on Optical Communications (ECOC), Vienna, Austria, 20–24 September 2009.
14. Shinada, S.; Furukawa, H.; Wada, N. Over 1-Tbit/s/port Polarization-Multiplexed DWDM/DQPSK Optical Packet Switching and Buffering. In Proceedings of the Optical Fiber Communications Conference (OFC), Los Angeles, CA, USA, 6–10 March 2011.

15. Shinada, S.; Furukawa, H.; Wada, N. 2.56 Tbit/s/port Dual-Polarization DWDM/NRZ-DQPSK Optical Packet Switching and Buffering. In Proceedings of the European Conference on Optical Communications (ECOC), Geneva, Switzerland, 18–22 September 2011.
16. Shinada, S.; Furukawa, H.; Wada, N. Huge capacity optical packet switching and buffering. *Opt. Express* **2011**, *26*, B406–B414. [[CrossRef](#)] [[PubMed](#)]
17. Delgado Mendinueta, J.M.; Puttnam, B.J.; Luis, R.S.; Shinada, S.; Wada, N. Fast Equalizer Kernel Initialization for Coherent PDM-QPSK Burst-Mode Receivers Based on Stokes Estimator. In Proceedings of the OSA Advanced Photonics, Rio Grande, PR, USA, 14–17 July 2013.
18. Shinada, S.; Delgado Mendinueta, J.M.; Wada, N. Over 10-Tbit/s/port Optical Packet Switching Using Polarization-Multiplexed DWDM/16-QAM Packets. In Proceedings of the Optical Fiber Communications Conference (OFC), San Francisco, CA, USA, 9–13 March 2014.
19. Xu, J.; Zhang, X.; Mork, J. Investigation of Patterning Effects in Ultrafast SOA-Based Optical Switches. *IEEE J. Quantum Electron.* **2010**, *46*, 87–94. [[CrossRef](#)]
20. Kamitani, N.; Yoshida, Y.; Kitayama, K. Experimental study on impact of SOA nonlinear phase noise in 40Gbps coherent 16QAM transmissions. In Proceedings of the European Conference on Optical Communications (ECOC), Amsterdam, The Netherlands, 16–20 September 2012.
21. Shinada, S.; Delgado Mendinueta, J.M.; Wada, N. Demonstration of a DWDM Polarization-Division Multiplexing 16QAM Optical Packet Switching Node with Packet Buffering. In Proceedings of the Optoelectronics and Communications Conference (OECC), Melbourne, Australia, 6–10 July 2014.
22. Shinada, S.; Delgado Mendinueta, J.M.; Luis, R.S.; Wada, N. Operation of a 12.8 Tbit/s DWDM Polarization Division Multiplexing 16-QAM Optical Packet Switching Node after 50 km Fiber Transmission. In Proceedings of the European Conference on Optical Communications (ECOC), Cannes, France, 21–25 September 2014.
23. Ossieur, P.; Ridder, T.D.; Bauwelinck, J.; Mélangé, C.; Baekelandt, B.; Qiu, X.-Z.; Vandewege, J.; Talli, G.; Antony, C.; Townsend, P.; et al. A 10 Gb/s Burst-Mode Receiver with Automatic Reset Generation and Burst Detection for Extended Reach PONs. In Proceedings of the Optical Fiber Communications Conference (OFC), San Diego, CA, USA, 22–26 March 2009.
24. Poehlmann, W.; Schmuck, H.; Bonk, R.; Pfeiffer, T. First 20 Gbit/s Burst-mode OOK Upstream with Direct Modulated Laser over up to 50 km Single Mode Fiber. In Proceedings of IEEE Photonics Networks Conference, Waikoloa, HI, USA, 2–6 October 2016.
25. Savory, S.J. Digital Coherent Optical Receivers: Algorithms and Subsystems. *IEEE J. Sel. Top. Quantum Electron.* **2016**, *16*, 1164–1179. [[CrossRef](#)]
26. Vacondio, F.; Simonneau, C.; Voicila, A.; Dutisseuil, E.; Tanguy, J.-M.; Antona, J.-C.; Charlet, G.; Bigo, S. Real time implementation of packet-by-packet polarization demultiplexing in a 28 Gb/s burst mode coherent receiver. In Proceedings of the Optical Fiber Communications Conference (OFC), Los Angeles, CA, USA, 4–8 March 2012.
27. Kikuchi, K.; Tsukamoto, S. Evaluation of Sensitivity of the Digital Coherent Receiver. *J. Lightwave Technol.* **2008**, *26*, 1817–1822. [[CrossRef](#)]
28. Maher, R.; Millar, D.; Savory, S.; Thomsen, B.J. Widely Tunable Burst Mode Digital Coherent Receiver with Fast Reconfiguration Time for 112 Gb/s DP-QPSK WDM Networks. *J. Lightwave Technol.* **2012**, *30*, 3924–3930. [[CrossRef](#)]
29. Geyer, J.; Hauske, F.; Fludger, C.; Duthel, T.; Schullien, C.; Kuschnerov, M.; Piyawanno, K.; van den Borne, D.; Schmidt, E.-D.; Spinnler, B.; et al. Channel parameter estimation for polarization diverse coherent receivers. *IEEE Photonics Technol. Lett.* **2008**, *20*, 776–778. [[CrossRef](#)]
30. Hauske, F.; Kuschnerov, M.; Spinnler, B.; Lankl, B. Optical performance monitoring in digital coherent receivers. *J. Lightwave Technol.* **2009**, *27*, 3623–3631. [[CrossRef](#)]
31. Agrawal, G.P. *Lightwave Technology Telecommunication Systems*; John Wiley & Sons: Somerset, NJ, USA, 2005.
32. Szafraniec, B.; Nebendahl, B.; Marshall, T. Polarization demultiplexing in Stokes space. *Opt. Express* **2010**, *18*, 17928–17939. [[CrossRef](#)] [[PubMed](#)]
33. Szafraniec, B.; Marshall, T.S.; Nebendahl, B. Performance Monitoring and Measurement Techniques for Coherent Optical Systems. *J. Lightwave Technol.* **2013**, *31*, 648–663. [[CrossRef](#)]

34. Borkowski, R.; Zibar, D.; Caballero, A.; Arlunno, V.; Tafur Monroy, I. Optical Modulation Format Recognition in Stokes Space for Digital Coherent Receivers. In Proceedings of the Optical Fiber Communications Conference (OFC), Anaheim, CA, USA, 19–21 March 2013.
35. Roman, S. *Advanced Linear Algebra*, 3rd ed.; Springer: New York, NY, USA, 2008.
36. Delgado Mendinueta, J.M.; Furukawa, H.; Shinada, S.; Wada, N. Multi-rate coherent burst-mode PDM-QPSK optical receiver for flexible optical networks. In Proceedings of the Optoelectronics and Communications Conference (OECC), Niigata, Japan, 3–7 July 2016.
37. Lee, S.J. A new non-data-aided feedforward symbol timing estimator using two samples per symbol. *IEEE Commun. Lett.* **2002**, *6*, 205–207.
38. Oerder, M.; Meyr, H. Digital Filter and Square Timing Recovery. *IEEE Trans. Commun.* **1998**, *36*, 605–612. [[CrossRef](#)]
39. Huang, L.; Lau, A.P.T.; Lu, C.; He, S. Performance analysis of blind timing phase estimators for digital coherent receivers. *Opt. Express* **2014**, *22*, 6749–6763. [[CrossRef](#)] [[PubMed](#)]
40. Viterbi, A.J.; Viterbi, A.M. Nonlinear Estimation of PSK-modulated carrier Phase with Application to Burst Digital Transmission. *IEEE Trans. Inf. Theory* **1983**, *29*, 543–551. [[CrossRef](#)]
41. Fatadin, I.; Ives, D.; Savory, S.J. Laser Linewidth Tolerance for 16-QAM Coherent Optical Systems Using QPSK Partitioning. *IEEE Photonics Technol. Lett.* **2010**, *22*, 631–633. [[CrossRef](#)]
42. Cincotti, G.; Wada, N.; Kitayama, K. Characterization of a full encoder/decoder in the AWG configuration for code-based photonic routers—Part I: Modeling and Design. *J. Lightwave Technol.* **2006**, *24*, 103–112. [[CrossRef](#)]
43. Wada, N.; Cincotti, G.; Yoshima, S.; Kataoka, N.; Kitayama, K. Characterization of a full encoder/decoder in the AWG configuration for code-based photonic routers—Part II: Experiments and applications. *J. Lightwave Technol.* **2006**, *24*, 113–121. [[CrossRef](#)]
44. Shinada, S.; Furukawa, H.; Wada, N. Demonstration of Flexible Optical Buffer based on  $1 \times 32$  Optical Switches and Fiber-Sheet Delay Lines. In Proceedings of the Optical Fiber Communications Conference (OFC), Anaheim, CA, USA, 19–21 March 2013.
45. Shinada, S.; Furukawa, H.; Wada, N. Investigation of Optical Buffer Capacity using Large-scale Fiber Delay Lines for Variable-length Optical Packet Switching. In Proceedings of the European Conference on Optical Communications (ECOC), London, UK, 22–26 September 2013.
46. Wang, J.; Speidel, J. 16QAM Symbol Timing Recovery in the Upstream Transmission of DOCSIS Standard. *IEEE Trans. Broadcast.* **2003**, *49*, 211–216. [[CrossRef](#)]



© 2017 by the authors. Licensee MDPI, Basel, Switzerland. This article is an open access article distributed under the terms and conditions of the Creative Commons Attribution (CC BY) license (<http://creativecommons.org/licenses/by/4.0/>).